



Shape optimization of axial groove miniature heat pipes

Petersen, Asger Bjerregaard; Sigmund, Ole; Andreasen, Casper Schousboe

Published in:
International Journal of Heat and Mass Transfer

Link to article, DOI:
[10.1016/j.ijheatmasstransfer.2025.128028](https://doi.org/10.1016/j.ijheatmasstransfer.2025.128028)

Publication date:
2026

Document Version
Publisher's PDF, also known as Version of record

[Link back to DTU Orbit](#)

Citation (APA):
Petersen, A. B., Sigmund, O., & Andreasen, C. S. (2026). Shape optimization of axial groove miniature heat pipes. *International Journal of Heat and Mass Transfer*, 256, Article 128028. <https://doi.org/10.1016/j.ijheatmasstransfer.2025.128028>

General rights

Copyright and moral rights for the publications made accessible in the public portal are retained by the authors and/or other copyright owners and it is a condition of accessing publications that users recognise and abide by the legal requirements associated with these rights.

- Users may download and print one copy of any publication from the public portal for the purpose of private study or research.
- You may not further distribute the material or use it for any profit-making activity or commercial gain
- You may freely distribute the URL identifying the publication in the public portal

If you believe that this document breaches copyright please contact us providing details, and we will remove access to the work immediately and investigate your claim.



Shape optimization of axial groove miniature heat pipes

Asger Bjerregaard Petersen^{ID*}, Ole Sigmund^{ID}, Casper Schousboe Andreasen^{ID}

Department of Civil and Mechanical Engineering, Technical University of Denmark, Kgs. Lyngby, 2800, Denmark

ARTICLE INFO

Keywords:

Heat pipe
Micro groove
Shape optimization

ABSTRACT

Flat miniature heat pipes (FMHPs) are compact, passive thermal management devices that leverage phase change to sustain high heat fluxes. Their performance is strongly influenced by the geometry of the internal wick structure, which governs capillary-driven liquid transport. This work presents a reduced-order numerical model for predicting the steady-state thermal performance of FMHPs with axially grooved wicks. The model captures key thermohydraulic phenomena while enabling efficient gradient-based shape optimization by simplifying the governing equations and linearizing the phase-change mass flux. The groove width is parametrized along the axial direction and optimized to maximize the heat transport capacity. Validation against experimental and high-fidelity numerical results demonstrates the model's accuracy and efficiency. Optimization results show that non-uniform groove profiles can significantly enhance performance, achieving up to 24% improvement in maximum heat input compared to uniform grooves, without increasing the device footprint. The study highlights the potential of shape optimization in advancing the design of high-performance FMHPs for electronics cooling and other heat-intensive applications.

1. Introduction

Effective thermal management is a central challenge in the design of micro- and miniature-scale electronic devices, as it directly influences system performance, reliability, and cost. With continued miniaturization, power densities have exceeded 190 W cm^{-2} [1], pushing conventional cooling strategies to their operational limits [2].

Flat miniature heat pipes (FMHPs) have emerged as efficient passive cooling solutions due to their high effective thermal conductivity and compact form factor. Their ability to handle large heat loads depends strongly on internal geometry, particularly the configuration of the wick which governs fluid transport efficiency. Consequently, maximizing heat transfer through optimal internal design is key to improving the thermal performance of FMHPs in demanding applications.

Cotter [3] introduced the concept of micro heat pipes and developed a numerical model to predict their thermal performance. Babin et al. [4] refined the one-dimensional steady-state model of Cotter by redefining the axial heat flux and accounting for the capillary limit. Khrustalev and Faghri [5,6] extended this model to include interfacial shear stress, working fluid charge, dedicated evaporation and condensation models and the boiling limit. Hopkins et al. [7] introduced the idea of micro-grooved wick structures combined with miniature vapor channels, greatly expanding the range of viable operating conditions.

The one-dimensional models have evolved steadily to include additional physical effects. Do et al. [8] accounted for axial wall temperature variations. More recently, Abolmaali et al. [9] incorporated refined

evaporation mass fluxes derived from two-dimensional cross-sectional multi-scale simulations [10,11], yielding improved accuracy in thermal predictions. Both Do et al. and Abolmaali et al. performed basic optimization of the grooved wick structure via parametric sweeps of geometric dimensions but did not employ formal optimization methods or shape variations.

Several high-fidelity models have been developed to better resolve spatial variations in heat and mass transport. Gökçe et al. [12] proposed a comprehensive three-dimensional model of the wall and a liquid filled groove from a flat grooved heat pipe under steady-state operation, which was implemented with finite difference, finite element and finite volume formulations. It was later accelerated in [13] to reduce computational cost. Another approach by Fang et al. [14] employed a 3D lattice Boltzmann model to study micro heat pipes with pinned and grooved wick structures. However, their simulations were constrained by limitations of the lattice Boltzmann model.

Despite increased interest in optimizing wick structures, many studies still rely on limited parameter sweeps. For instance, the geometric explorations by Do et al. [8] and Abolmaali et al. [9] represent only a subset of the design space. An exception is the work by Alam et al. [15], who use ant colony optimization to minimize heat pipe mass under multiple constraints. However, their approach is based on simplified limits and does not capture detailed physical behavior, limiting the scope of design insights. In contrast, the high-fidelity models by Gökçe

* Corresponding author.

E-mail address: abape@dtu.dk (A.B. Petersen).

et al. [13], Fang et al. [14] and Abolmaali et al. [9] provide greater physical accuracy but are computationally expensive, making them impractical for optimization. As a result, there is a gap between physical fidelity and optimization efficiency. Gradient-based optimization methods are underutilized in the field of micro and miniature heat pipes. However, they are well-suited for heat transfer applications, with some considerations, as reviewed by Dbouk [16]. These techniques have led to novel solutions in related systems such as vapor chambers [17,18] and porous wick heat pipes [19], demonstrating the potential of employing optimization for micro and miniature heat pipes.

To address these challenges, we propose a reduced-order model that bridges the gap between high-fidelity simulation and gradient-based optimization. The model uses specific physical and numerical simplifications that significantly reduce computational cost while preserving the thermal performance trends observed in more detailed simulations. By eliminating some couplings, non-linearities and adopting linearized terms our formulation ensures smooth, stable gradients suitable for use with optimization algorithms.

The proposed model includes two novel features to account for geometric changes in the wick structure. It determines the non-trivial location of the maximum meniscus curvature and incorporates the derivative of geometric cross-sectional area. These additions enhance the model's sensitivity to shape variations and support gradient-based optimization. This balance of accuracy, robustness, and efficiency makes the model ideally suited for shape optimization of miniature heat pipes.

The paper is structured as follows. Section 2 presents the governing equations and numerical formulation of the reduced-order model. Section 3 provides model validation against literature, and optimization results. Section 4 summarizes the conclusions and discusses directions for future work.

2. Method

2.1. Working principles for a FMHP

A wicked FMHP consists of an outer wall, a wick structure and a vapor channel as shown in Fig. 1. It is partially filled with a working fluid that transfers heat through the latent heat of vaporization. At the heat source, the working fluid within the wick evaporates into the vapor channel, consuming thermal energy and generating a pressure-driven vapor flow towards the heat sink. Upon reaching the heat sink, the vapor condenses on the solid wall, releasing thermal energy. The resulting liquid is then drawn back into the micro grooves and transported back to the heat source via capillary action, thus sustaining the heat transfer cycle. The lower part of Fig. 1 illustrates a section view of the FMHP, visualizing fluid circulation driven by heat flux.

2.2. Assumptions and simplifications

The proposed model aims to capture the primary effects of a micro-grooved wick structure on thermal performance while ensuring swift evaluation. To achieve this, a lower-fidelity formulation of the governing equations is adopted.

A steady-state approach is adopted to reduce model complexity, which is sufficient for estimating performance limits [4].

The model domain is reduced from three dimensions to one dimension along the axial x direction, due to the large aspect ratio of the FMHP geometry and the high degree of uniformity in cross-sectional temperature, vapor and liquid velocities. Temperature variations along x account for the entire solid cross section, while vapor-phase variations also follow a 1D treatment along the vapor channel. The liquid domain is simplified to axial variation within a single representative liquid filled groove.

Both vapor and liquid flows are assumed incompressible and laminar, as the observed Mach number for the vapor is $Ma \ll 1$ and both phases exhibit Reynolds numbers below the laminar-turbulent

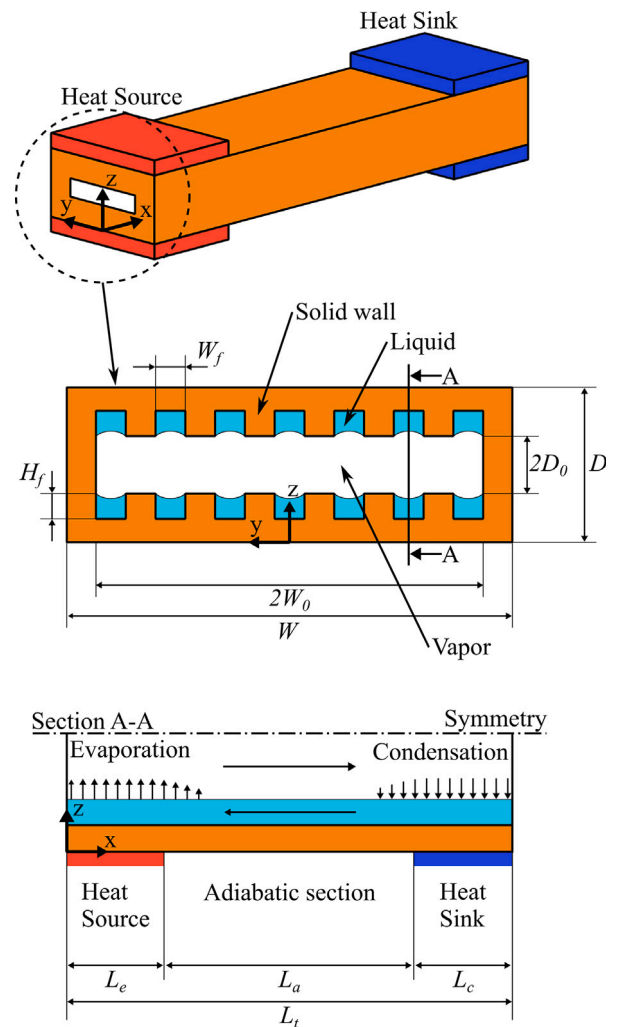


Fig. 1. Stylized depiction of a flat miniature heat pipe micro groove wick structure.

transition threshold, $Re < 2300$. As a result, the model cannot capture the sonic limit because compressibility, which is essential for describing such flow conditions, is not included.

The meniscus curvature in the axial direction is assumed negligible due to the extreme aspect ratio (1:600) of the liquid grooves.

Under steady-state conditions, the cross-sectional shape of the meniscus is assumed circular, corresponding to the minimum energy configuration of the intrinsic meniscus at mechanical equilibrium.

It is further assumed that the meniscus remains pinned at the upper corners of the liquid grooves, such as Khrustalev & Faghri [6]. This simplification has minimal influence on accuracy, as the deviation primarily occurs near the evaporator end ($x = 0$), where the liquid velocity approaches zero, and significantly reduces implementation complexity. However, by keeping the meniscus pinned at the upper corners, the model cannot represent a receding meniscus or evaporator dryout directly.

Assuming small meniscus curvature allows the associated changes in vapor and liquid cross-sectional areas to be neglected. This facilitates partial decoupling of the governing equations, further reducing numerical complexity and evaluation time.

Temperature variation in the solid wall is assumed to be primarily governed by conduction, as well as heat fluxes associated with

phase change, external heating, and cooling. These effects are considered dominant compared to conduction and convection in the vapor and liquid domains, which are limited by low velocities, thermal conductivities, and heat capacities.

The working fluid charge is assumed optimal, ensuring the grooves are neither underfilled nor overfilled. This avoids complications related to dryout or liquid blockage and ensures consistent capillary-driven flow throughout the wick.

Due to the dominance of thin-film evaporation and condensation near the contact line, the thermal resistance across the liquid film is assumed negligible. Consequently, the local solid wall temperature is used directly as the meniscus surface temperature when calculating the superheat that drives phase-change mass fluxes.

To enable a more computationally efficient and differentiable model, the evaporation and condensation mass fluxes are assumed to depend linearly on the local wall superheat. This assumption is derived from a linearized approximation of a previously established, highly coupled nonlinear correlation [9], and is found to preserve the essential physical behavior over the relevant operating range.

2.3. Governing equations

The governing equations are derived based on the assumptions and simplifications outlined above. A stylized depiction of the model domains are shown in Fig. 1, which also show geometric parameters. The model is split into three domains: Solid wall, vapor channel and a single representative liquid filled groove.

2.3.1. Thermal model

In the proposed model axial variation of wall temperature is accounted for, as it is relatively large for miniature heat pipes. The conservation of energy is stated as, [8]:

$$k_s A_s \frac{\partial^2 T_s}{\partial x^2} = N h_{fg} \dot{m}'_{pc} - q''_w P_w \quad (1)$$

where k_s is the thermal conductivity of the solid, A_s the cross sectional area of the solid, T_s the solid temperature, N the total number of liquid filled grooves, h_{fg} the latent heat of vaporization for the working fluid, \dot{m}'_{pc} the mass flux due to phase change across the meniscus, q''_w the external heat flux applied to the solid wall and P_w the external wall perimeter subject to heat flux q''_w .

The cross sectional area is defined as $A_s = DW - 4D_0W_0 - NW_fH_f$, where D is the total height of the heat pipe, W the total width, D_0 the half height of the vapor channel, W_0 the half width of the vapor channel, W_f the liquid groove width, H_f the liquid groove height. All dimensions are visualized in Fig. 1.

The external heat flux is modeled as prescribed heat flux into the evaporator and out of the condenser. The external heat flux is:

$$q''_w = \begin{cases} \frac{Q_{in}}{P_w L_c} & 0 \leq x < L_e \\ 0 & L_e \leq x < L_e + L_a \\ -\frac{Q_{in}}{P_w L_c} & L_e + L_a \leq x < L_l \end{cases} \quad (2)$$

where Q_{in} is the total heat input and the lengths L_e , L_a , L_c and L_l are illustrated in Fig. 1. This definition of q''_w is independent of the working temperature T_v . By prescribing a constant T_v the material properties can be assumed constant, due to negligible temperature variations in the fluids.

To model no energy transfer across the ends the boundary conditions for the solid temperature are given as:

$$\frac{\partial T_s}{\partial x} \Big|_{x=0} = \frac{\partial T_s}{\partial x} \Big|_{x=L_l} = 0 \quad (3)$$

2.3.2. Phase change mass flux

In literature multiple approaches to accurately capture the mass flux due to evaporation and condensation in micro grooves have emerged [10,11,20]. A correlation was developed by Abolimaali et al. in [9], based on a parameter sweep performed using the high-fidelity numerical models reported in [10] and [11]. These models accurately capture evaporation and condensation in grooves but involve substantial computational cost. The proposed correlation reproduces their predictive accuracy while offering the computational efficiency of empirical formulations. The correlation for evaporation mass flux of water in a copper groove, [9], yields:

$$\dot{m}'_{evp} [\text{mg m}^{-1} \text{s}^{-1}] = 6.4496 T_s^{0.8281} \left(\frac{2}{\kappa W_f} \right)^{-0.0132} W_f^{0.1976} \quad (4)$$

which is valid within the following range of parameters: $0.01 \leq T_s$ [K] ≤ 12 , $1.0 \leq \frac{2}{\kappa W_f}$ [-] ≤ 10.0 , and $160 \leq W_f$ [μm] ≤ 240 . Here κ is the curvature of the meniscus. This correlation is significantly simpler than most models. However, it still contains a significant number of non-linear couplings between groove width, temperature of solid and curvature of meniscus.

As the goal is to ensure usable accuracy, swift evaluation and differentiable governing equations, the correlation is replaced with a linearized term. The dominant relationship within the correlation is the temperature-mass flux term, thus the linearized term is defined as:

$$\dot{m}'_{pc} = \alpha T_i \approx \alpha T_s \quad (5)$$

where α is a constant for scaling the mass flux-solid temperature relationship and T_i is the meniscus interface temperature. Assuming most evaporation occurs in the thin-film regime and at small thin-film thickness the temperature difference between T_i and T_s is assumed negligible. The linearized model, Eq. (5), leads to an error in the mass flux term, which is shown in Fig. 2. The primary source of the error is a lack of non-linear relationship between T_s and \dot{m}'_{pc} , however the benchmark results in Section 3.1 indicates that this approach is acceptable.

2.3.3. Hydrodynamic model

The hydrodynamic model covers the mass continuity of vapor and liquid as well as the differential form of the Young–Laplace equation, which is derived from the vapor and liquid momentum continuities. The mass continuity equations for the vapor and liquid flows are expressed as, [21]:

$$A_v \frac{\partial u_v}{\partial x} = N \frac{\dot{m}'_{pc}}{\rho_v} \quad (6)$$

$$\frac{\partial A_l u_l}{\partial x} = -\frac{\dot{m}'_{pc}}{\rho_l} \quad (7)$$

where A is the cross-sectional area, u the mean axial fluid velocity and ρ the fluid density. The subscripts v and l indicate vapor and liquid, respectively.

The net axial mass flow rate along the heat pipe is zero, as the mass source terms $-\dot{m}'_{pc}$ from each of the N grooves are balanced by $N\dot{m}'_{pc}$ in the vapor channel.

Since the wick structure is subject to optimization, the area A_l is included in the derivative. However, the change in cross sectional areas A_v and A_l caused by changes to the vapor–liquid meniscus are neglected. The areas are defined as: $A_v = 4D_0W_0$ and $A_l = W_fH_f$.

Based on the assumptions for vapor the Navier–Stokes equation simplifies to:

$$A_v \frac{\partial \rho_v u_v^2}{\partial x} = -A_v \frac{\partial p_v}{\partial x} + A_v \mu_v \frac{\partial^2 u_v}{\partial x^2} \quad (8)$$

where p_v is the vapor pressure and μ_v is the dynamic viscosity of vapor. This form includes inertia, pressure force and viscous shear. The viscous shear is replaced by an approximation of the wall shear stress:

$$A_v \frac{\partial \rho_v u_v^2}{\partial x} = -A_v \frac{\partial p_v}{\partial x} - \tau_{vw} P_{vw} \quad (9)$$

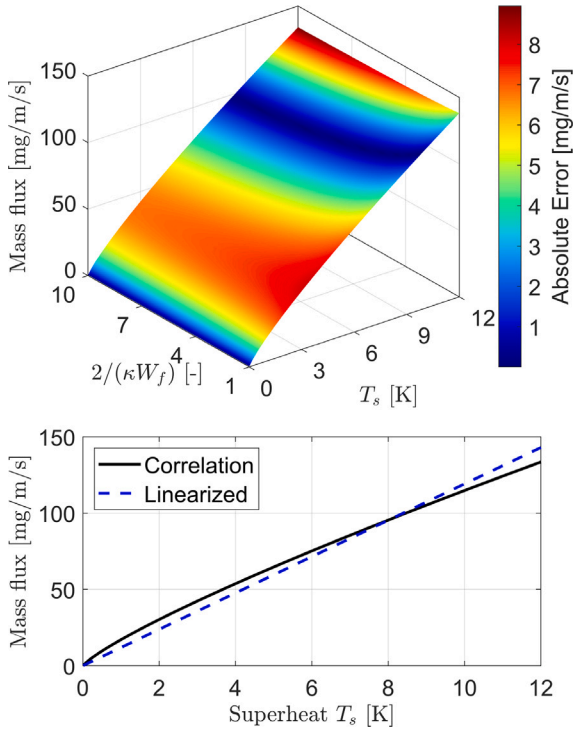


Fig. 2. Comparison of evaporative mass flux correlation and linearized mass flux at $W_f = 160 \mu\text{m}$. And cross section of correlation at $2/(\kappa W_f)^4 = 7$ compared with linearized model.

where τ_{vw} is the shear stress between the vapor and the wall and P_{vw} is the wetted perimeter. Isolating the pressure gradients and expanding the inertia term leads to, [9]:

$$\frac{\partial p_v}{\partial x} = -2\rho_v u_v \frac{\partial u_v}{\partial x} - \frac{\tau_{vw} P_{vw}}{A_v} \quad (10)$$

The scaling between the vapor and liquid velocities is closely related to the scaling between vapor and liquid density, thus velocity scaling is on the order of 100–1000, [22]. Due to the large difference in the velocities the liquid is perceived as stationary from the vapor and part of the wetted perimeter. For rectangular conduits the wall shear stress can be expressed as, [23]:

$$\tau_{vw} = \frac{24\mu_v u_v}{\pi^2 W_0} \frac{\sum_{n=1}^{\infty} \frac{(-1)^{n-1}}{(2n-1)^2} \tanh\left(\frac{(2n-1)\pi D_0}{2W_0}\right)}{1 - \frac{192}{\pi^5} \frac{W_0}{D_0} \sum_{n=1}^{\infty} \frac{1}{(2n-1)^5} \tanh\left(\frac{(2n-1)\pi D_0}{2W_0}\right)} \quad (11)$$

Applying the same method to the Navier–Stokes equation for the liquid flow leads to, [9]:

$$\frac{\partial p_l}{\partial x} = -\frac{2\mu_l u_l}{D_{hl}^2} (fRe)_l \quad (12)$$

where p_l is the liquid pressure, μ_l is the liquid dynamic viscosity, D_{hl} is the hydraulic diameter and $(fRe)_l$ is the Poiseuille number. For the liquid momentum equilibrium, inertia is negligible due to low speeds, [5].

The velocity profile within a closed groove is shown in Fig. 3 center. This assumes a stationary boundary between vapor and liquid. However, due to velocity scaling the vapor is perceived as a significant shear stress at the vapor–liquid interface affecting liquid flow, as shown in Fig. 3 right. The effect of accounting for the shear stress on the vapor–liquid interface in the fRe formulation is shown in Fig. 3 left. For wider grooves the shear stress increases the flow resistance significantly.

This effect is accounted for by a special formulation of the Poiseuille number:

$$fRe = \frac{24 \left(1 + \frac{\tau^* W_f^2}{12 H_f^2} \left(1 - \frac{96}{\pi^4} \sum_{n=0}^{\infty} \frac{1}{(2n+1)^4} \operatorname{sech}\left(\frac{(2n+1)\pi H_f}{W_f}\right) \right) \right)}{\left(1 + \frac{W_f}{2H_f} \right)^2 \left(1 - \frac{96 W_f}{\pi^5 H_f} \sum_{n=0}^{\infty} \frac{1}{(2n+1)^5} \tanh\left(\frac{(2n+1)\pi H_f}{W_f}\right) \right)} \quad (13)$$

where τ^* is the dimensionless shear stress as shown in Fig. 3 and defined as:

$$\tau^* = \frac{H_f \tau_{vi}}{\mu_l u_l} \quad (14)$$

This formulation was defined as “DiCola’s model” by Schneider and DeVos [24]. For various groove geometries Shah & London, [25], provides fRe formulations without shear stress at the vapor–liquid interface. Combined with Schneider and DeVos’ correction factor, [24], it is possible to model non-rectangular grooves.

To reduce computational complexity the momentum equations for both fluid phases are rearranged and inserted in the differential form of the Young–Laplace equation to reduce the required degrees of freedom from six to four by collapsing the pressures and meniscus curvature into just the curvature.

The differential form of the Young–Laplace equation is defined as, [26]:

$$\sigma \frac{\partial \kappa}{\partial x} = \frac{\partial p_v}{\partial x} - \frac{\partial p_l}{\partial x} \quad (15)$$

where σ is the surface tension.

Inserting Eqs. (10) and (12) into (15) leads to the final equation:

$$\frac{\partial \kappa}{\partial x} = \frac{1}{\sigma} \left(\frac{2\mu_l u_l}{D_{hl}^2} (fRe)_l - 2\rho_v u_v \frac{\partial u_v}{\partial x} - \frac{\tau_{vw} P_{vw}}{A_v} \right) \quad (16)$$

To finalize the hydrodynamic model, the boundary conditions, need to be defined. For the continuity Eqs. (6) and (7) the boundary conditions are enforced as no flow over the boundary:

$$u_l|_{x=0} = u_v|_{x=0} = u_l|_{x=L_t} = u_v|_{x=L_t} = 0 \quad (17)$$

The boundary conditions for curvature of the meniscus are derived from the contact angle. The contact angle is based on the working fluid and solid material combination. The contact angle is defined as:

$$\cos \gamma = \frac{1}{2} W_f \kappa \quad (18)$$

where γ is the contact angle, as shown in Fig. 4, and is clearly dependent on the curvature of meniscus and local groove width.

For a uniform groove the curvature at maximum heat flux is defined by γ_{min} at the evaporator end ($x = 0$), which is the boundary condition found in literature, see Do et al. [8] or Abolmaali et al. [9].

For non-uniform grooves the minimum contact angle can occur elsewhere within the groove, typically within the evaporator section. For simplicity and by letting the optimizer implicitly solve for optimal fluid charge the curvature at the condenser end ($x = L_t$) is set to zero, similar to the boundary condition of Babin et al. [4]. Q_{in} scales with $\kappa|_{x=L_t}$ as the value directly affects the available pressure drop from capillarity. For $\kappa|_{x=L_t}$ larger than zero the pressure drop is smaller thus reducing Q_{in} . The effect is limited to scaling Q_{in} but shows no effect on the optimization problem.

The final set of governing equations are combined to a set of residual equations, Eq. (19), which allows for compact notation of the governing equations in the following sections.

$$\mathbf{R} = \begin{bmatrix} k_s A_s \frac{\partial^2 T_s}{\partial x^2} - N h_{fg} \dot{m}'_{pc} + q''_w P_w \\ A_v \frac{\partial u_v}{\partial x} - N \frac{\dot{m}'_{pc}}{\rho_v} \\ \frac{\partial A_l u_l}{\partial x} + \frac{\dot{m}'_{pc}}{\rho_l} \\ \frac{\partial \kappa}{\partial x} - \frac{1}{\sigma} \left(\frac{2\mu_l u_l}{D_{hl}^2} (fRe)_l - 2\rho_v u_v \frac{\partial u_v}{\partial x} - \frac{\tau_{vw} P_{vw}}{A_v} \right) \end{bmatrix} = \mathbf{0} \quad (19)$$

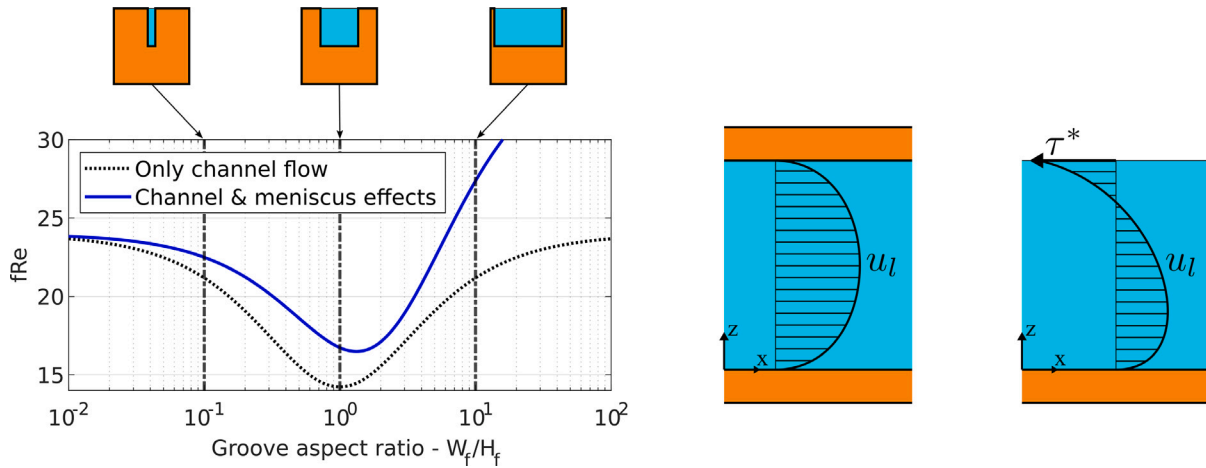


Fig. 3. Comparison of fRe models for channel flow with and with out meniscus effects.

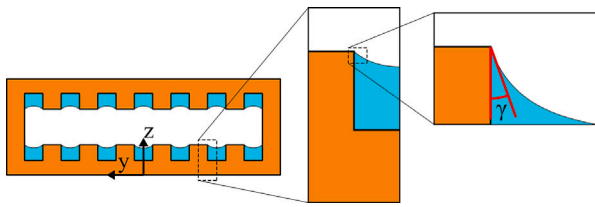


Fig. 4. Definition of the contact angle γ .

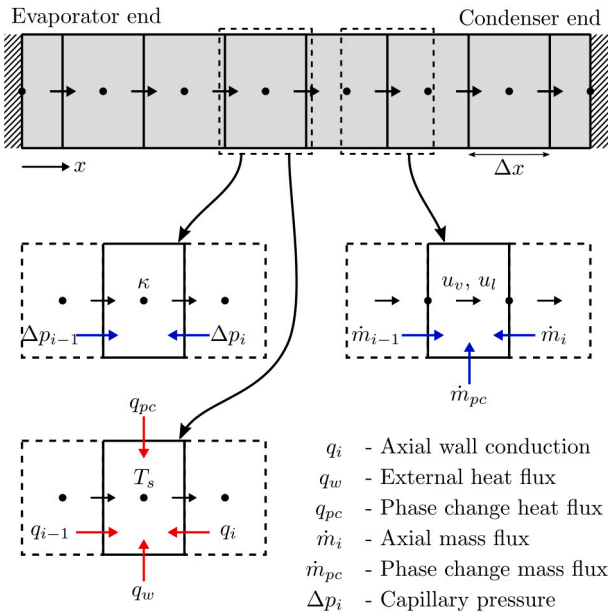


Fig. 5. Representation of staggered grid system.

2.3.4. Solution procedures

In literature the governing equations have been solved using explicit integration [8,26] and a combination of implicit and explicit methods [9,21]. Due to the linearized mass flux term from (5), a fully implicit finite volume method is adopted to solve the system of equations, (19).

The discretization is illustrated in Fig. 5 showing the staggered grid with face fluxes for the different cells, where curvature and temperature are collocated and offset with respect to velocities.

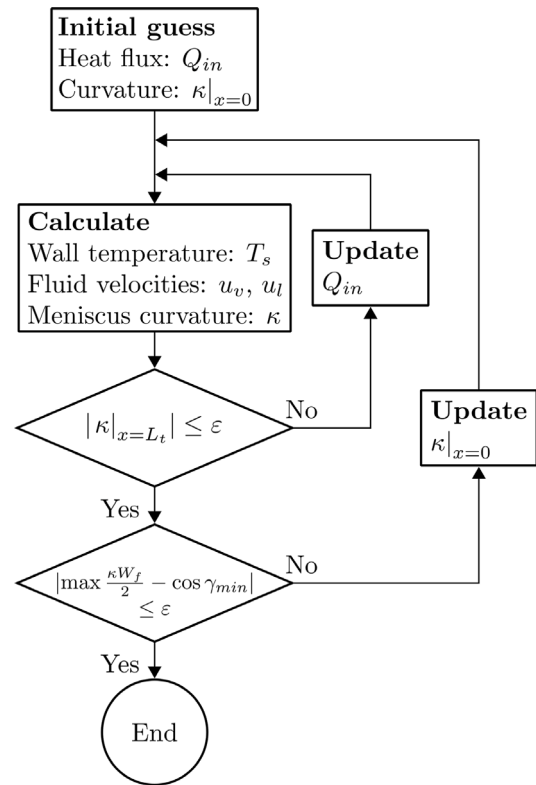


Fig. 6. Flow chart over iterative solution procedure.

Due to the linearized mass flux term, the governing equations are weakly coupled, for a given Q_{in} . The thermal problem is independent, the mass continuities are weakly coupled to the temperature field, and the Young–Laplace equation is weakly coupled to the mass continuities. Due to the order of dependencies, a sequential solution strategy is employed. The solution scheme begins with the solution of Eq. (1), which yields the temperature field T_s . From this temperature distribution, the mass flux associated with phase change, \dot{m}_{pc} , is determined. This flux is subsequently introduced as a source term in Eqs. (6) and (7), which are solved to obtain the vapor and liquid velocity fields. The computed velocities, that satisfy net axial mass balance, are then employed in Eq. (16) to evaluate the curvature of the meniscus.

Despite the linearized residual two sets of iterations are required to determine the maximum heat input. The inner iterations find the

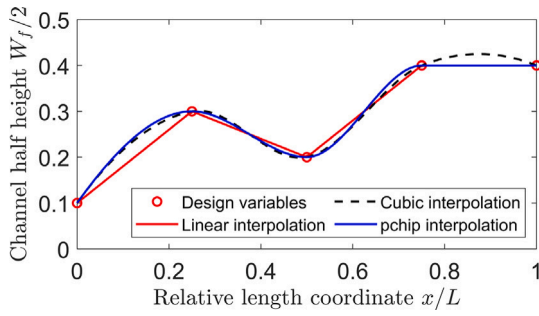


Fig. 7. Demonstration of interpolation schemes for $n_\psi = 5$ design nodes.

maximum Q_{in} by updating the current Q_{in} to enforce the boundary condition of $\kappa|_{x=L_t} = 0$. The outer iterations adjust the curvature of the meniscus at the evaporator end, $\kappa|_{x=0}$, to ensure the minimum contact angle is not exceeded. The convergence criteria are set to enforce the boundary conditions with a tolerance of $\epsilon = 10^{-4}$.

Both sets of iterations use Newton–Raphson iterations with first order finite difference gradients with a fixed perturbation of 10^{-4} W and radians respectively.

Fig. 6 shows the flow chart for solving the governing equations for a general groove geometry. The solution procedure finds the evaporator end curvature, κ_e , and the total heat input Q_{in} that satisfy all boundary conditions, based on an initial guess of κ_e and Q_{in} .

To reach convergence the solution procedure uses less than 10 outer iterations. For each outer iteration, less than 5 inner iterations are required. The low number of evaluations and fast computation result in a total solution time of approximately 1–2 min, which is significantly faster than methods found in literature, i.e. Gökçe et al. [13] with a runtime of 2 h. However the proposed procedure is lower fidelity so axial variations are of lower accuracy and cross sectional variations are not accounted for.

2.3.5. Parametrization for optimization

To ensure a simple optimized groove geometry, for ease of manufacturing, the optimization is limited to the axial groove width distribution $W_f(x)$.

To allow for axial width distribution of $W_f(x)$, a naive approach would be to let the value of $W_{f,i}$ in each node i be the design variables, similar to grid based shape optimization methods such as [27].

However, to ensure the assumption of negligible meniscus curvature along the x -direction it is important that the cross-sectional area of the liquid filled groove varies slowly. This is important as sudden changes or jumps in $W_f(x)$ cause kinks in the x -direction curvature, which corresponds to large or infinite curvature.

Fig. 7 shows that a piecewise linear interpolation scheme leads to kinks at the design nodes. A cubic spline interpolation shows a smooth curve with overshooting. A monotone piecewise cubic interpolation, [28], shows a curve with no overshooting while being smooth throughout the heat pipe and ensures the width at design nodes location are local extremum.

To avoid excessive curvature in the x -direction, the variation of $W_f(x)$ is defined using a few equally spaced design nodes and connected with monotone piecewise cubic interpolation to ensure slow and smooth changes between design nodes. For the implementation this is achieved by using the “pchip” interpolation scheme available in MATLAB. The groove width at the design nodes location is given as:

$$W_f = W_{min} + (W_{max} - W_{min})\psi \quad (20)$$

where W_{min} is the lower limit for the groove width and W_{max} is the upper limit for the groove width and ψ is the design variable.

Table 1

Dimensions of reference flat miniature heat pipe considered from [7].

Parameter	Value	Unit
W	13.41	mm
D	8.92	mm
W_0	4.875	mm
D_0	0.61	mm
H_f	0.42	mm
W_f	0.2	mm
N	62	–
L_e	15.6	mm
L_a	70	mm
L_c	34.4	mm

Table 2

Constants and material properties of working fluid and solid at saturation temperature $T_v = 80$ °C.

Parameter	Value	Unit
Liquid density (ρ_l)	971.77	kg m ⁻³
Vapor density (ρ_v)	0.2937	kg m ⁻³
Liquid viscosity (μ_l)	$3.5404 \cdot 10^{-4}$	Pa s
Vapor viscosity (μ_v)	$1.1539 \cdot 10^{-5}$	Pa s
Surface tension (σ)	0.0627	N m ⁻¹
Latent heat (h_{fg})	2307990	J kg ⁻¹
Thermal conductivity (k_s)	400	W m ⁻¹ K ⁻¹
Contact angle (θ_{min})	33	°

2.3.6. Optimization problem and sensitivities

With the groove width parametrization defined, the optimization problem is formulated. The goal is to increase the maximum total heat input. The optimization problem is thus defined as:

$$\begin{aligned} \max_{\psi \in \mathbb{R}^{n_\psi}} & : Q_{in} \\ \text{subject to} & : \mathbf{R} = \mathbf{0} \\ & 0 \leq \psi \leq 1 \end{aligned} \quad (21)$$

where \mathbf{R} is the residual from (19) and ψ is a vector of n_ψ equally spaced width design variables. The optimization problem is solved in a nested formulation where (19) is solved in every iteration and the Method of Moving Asymptotes (MMA) optimizes ψ based on sensitivity information, [29].

Due to the relatively low number of design variables and the two set of iterations in the solver it is chosen to use finite difference for calculating the sensitivities required to solve the optimization problem with MMA.

First order forward finite differencing proved inadequate for calculating sensitivities for the optimization problem. As the step size decreased the truncation error did not reach an acceptable level prior to the onset of significant subtractive cancellation errors. To achieve accurate sensitivities the method of complex step was used, [30]. A perturbation of 10^{-8} was chosen as it was the largest possible perturbation, which still ensures accurate sensitivities.

3. Results

This section is split into two subsections. First the proposed numerical model is benchmarked against an experiment and a numerical study to verify its ability to capture physics. Secondly the optimization problem is studied for various material properties and geometries to examine the optimal wick structure and its dependencies on material properties and geometries.

3.1. Benchmark

The proposed model is verified against existing numerical and experimental results from literature. Two benchmarks are covered in this

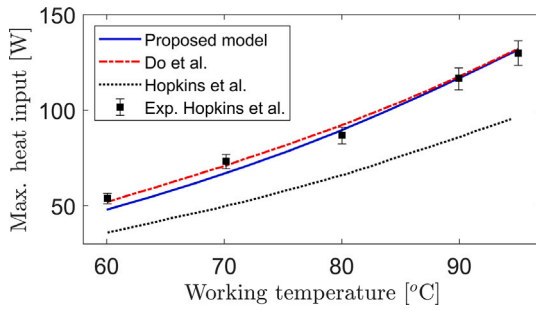


Fig. 8. Maximum heat input prediction for different working temperatures of the proposed model compared with Do et al. [8] and Hopkins et al. [7].

section. First a comparison to numerical and experimental work for a uniform groove wick structure. Second a comparison to numerical work on non-uniform groove wick structures.

3.1.1. Uniform groove wick structure

The experimental work conducted by Hopkins et al. [7] is used as a benchmark for the proposed numerical model. The considered heat pipe dimensions are listed in Table 1 and material properties at $T_v = 80\text{ }^\circ\text{C}$ are listed in Table 2. Appendix includes the complete table of material properties for a selection of T_v . Based on the complete data a cubic interpolation is used to recover material properties in the T_v range of 60–95 $^\circ\text{C}$. The validation is based on the relationship between working temperature and maximum heat input.

Due to thermal resistance of the heat sink attached to the condenser region, the operating temperature T_v typically exceeds ambient conditions. The specified range for T_v is considered representative of typical scenarios in consumer electronics.

To adjust the prediction accuracy of the proposed model a scaling term of the external wall flux is introduced, which is defined as:

$$q''_{w,adjusted} = \beta q''_w \quad (22)$$

where β is a constant, that is found by minimizing the mean error between the predicted heat input and the experimental values from Hopkins et al. [7]. With the adjustment factor $\beta = 0.5323$ the proposed model performs similar to the experimental reference and the numerical model of Do et al. [8], as seen in Fig. 8.

3.1.2. Non-uniform groove wick structure

The numerical parameter sweep conducted by Abolmaali et al. [9] is used as another benchmark for the proposed model. The parameter sweep is based on the flat miniature heat pipe covered in Section 3.1.1. The converging groove geometry is shown in Fig. 9 with relevant dimensions. The benchmark keeps a constant groove width $W_{f1} = 200\text{ }\mu\text{m}$ in the condenser half of the groove while utilizing a converging and diverging groove in the evaporator half as shown in Fig. 9. The evaporator end groove width, W_{f2} , is subjected to a sweep from 160 μm to 220 μm . The target is to ensure that the proposed model captures the trend in max heat input for the sweep, while maintaining sufficient accuracy for the maximum heat input prediction.

From Fig. 10 it is seen that the proposed model captures the effect of a converging and diverging groove and shows decent agreement with the results of Abolmaali et al. [9].

For evaporation Abolmaali et al. account for effects in the evaporating thin-film by a 4th order ordinary differential equation (ODE) and evaporation from the intrinsic meniscus with a 2D CFD analysis coupled to the thin-film ODE. For condensation they model the condensation on top of the fins as well as condensation on the bulk meniscus with similar ODEs to the thin-film evaporation. A deviation is expected since Abolmaali et al. model evaporation and condensation with highly sophisticated methods unlike the proposed linear term, which lacks the high fidelity found in Abolmaali et al. [9,11].

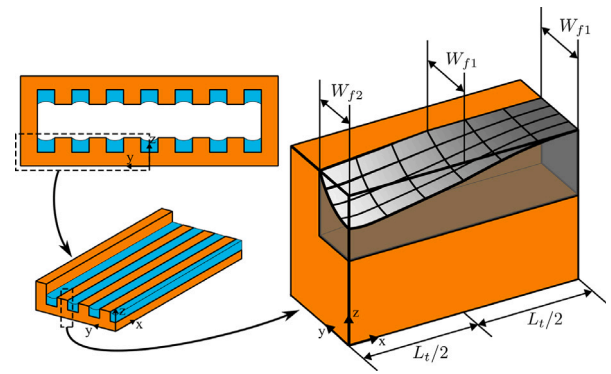


Fig. 9. Geometry of parameter sweep by Abolmaali et al..

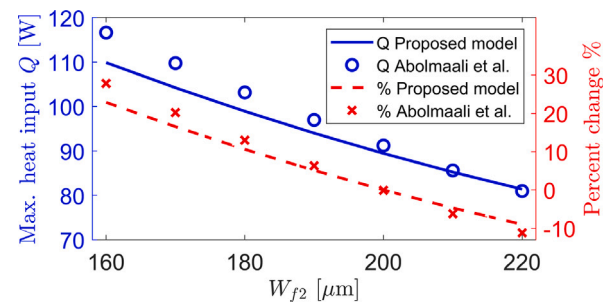


Fig. 10. Variation of the maximum heat input of flat heat pipe with W_{f2} for fixed W_{f1} . Comparison between present model and Abolmaali et al. [9].

Table 3
Parameters for optimization.

Parameter	Value	Unit
W_{min}	160	μm
W_{max}	220	μm
n_ψ	5	–

3.2. Optimization results and discussion

This section presents the results of optimization applied to the reference heat pipe from [7]. The primary goal of this section is to assess both the performance and sensitivity of the results to operating and geometric parameters.

The first subsection addresses the baseline maximization problem, establishing the effectiveness of the optimization approach in improving heat pipe performance under nominal conditions. The second subsection examines the influence of working temperature, where changes in material properties affect the optimization outcome. The third subsection evaluates the role of the number of design variables as a means of assessing convergence behavior and solution robustness. Finally, the influence of evaporator length is analyzed to demonstrate the effect of geometric modifications on the optimization process and resulting performance.

3.2.1. Maximization of maximum heat input

This section employs the optimization problem (21), on the reference copper–water heat pipe with geometry and material properties from Table 1 and 2, respectively. The reference heat pipe has a uniform groove width of $W_f = 200\text{ }\mu\text{m}$. The groove width design is limited to five design variables and bounds on the groove width as shown in Table 3.

The uniform reference grooved wick structure is shown alongside the converging and optimized groove structures in Fig. 11a and b respectively. Fig. 11c shows the optimized wick with bounds from

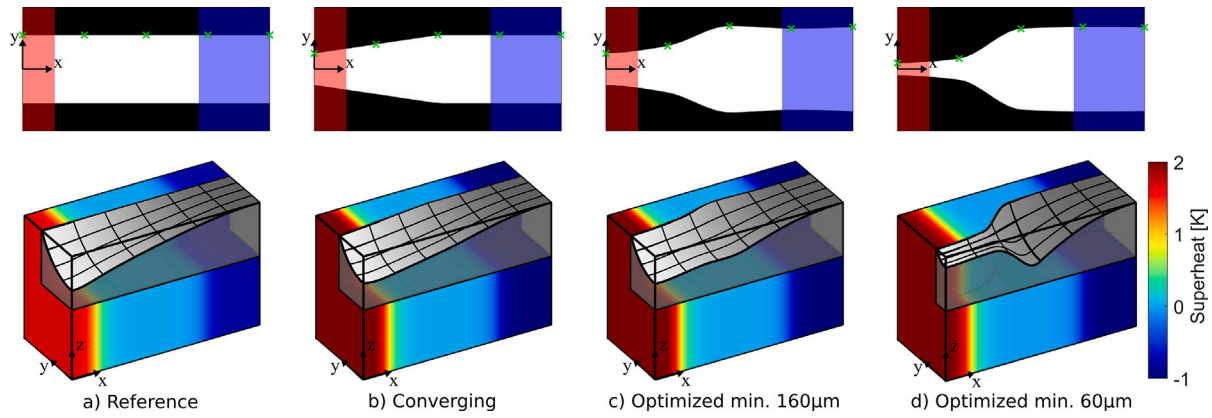


Fig. 11. Comparison of groove width distribution for the reference heat pipe of Hopkins et al. [7], converging distribution of Abolmaali et al. [9] and the optimized groove width distribution with $n_w = 5$ design variables. The top down projection is shown for a full groove with aspect ratio of 2 : 1 and the design variables marked by green crosses. The 3D visualizations show temperature distributions and local meniscus shapes using stylized half-grooves with an artificial aspect ratio of $[x, y, z] = [2.3, 1, 1.5]$, chosen for interpretability. In contrast, the modeled physical devices have an aspect ratio of [400, 1, 12.8]. Meniscus displacement is exaggerated by a factor of five for visualization.

Table 3, while Fig. 11d shows an optimized wick for a smaller lower bound of 60 μm . The design variables for each groove geometry are shown on the top-down projections in Fig. 11. The grooves are shown with an aspect ratio of 2 : 1, while the physical aspect ratio is 400 : 1.

The optimized wick structures exhibit similarities to the converging grooved wick structure, with both configurations featuring a minimum width at the evaporator end ($x/L_t = 0$) that gradually increases toward a maximum width at approximately $x/L_t = 0.5$, as shown in the top of Fig. 11.

Fig. 11c and d present the optimized groove width distributions, both of which exhibit a distinct bottle-like shape characterized by a narrow neck at the evaporator end and a wider body toward the condenser. These distributions share similarities with the previously studied converging groove width profile, which features a linearly expanding neck. In contrast, the optimized profiles display a non-linear expansion. Toward the condenser end, the groove width stabilizes, showing an almost constant value with only minor oscillations.

For the optimized grooved wick structure, shown in Fig. 11c, the objective evolution shows that the optimizer increases the maximum heat input followed by a plateau, as seen in Fig. 12. This indicates that a maximum is quickly found then refined. The total number of iterations is low, as expected, due to the small number of design variables and the simple geometry.

The thermal performance improvement of the optimized wick structure wrt. the reference is significant while only a small improvement is achieved wrt. the converging wick structure, as seen in Table 4. This indicates that the most important feature in the optimized wick structure is the narrow evaporator end and wide groove away from the region of evaporation, as this maximizes capillary pressure while minimizing pressure drop in the wick structure.

As shown in Fig. 11c and d, the optimized groove width distributions exhibit noticeable width variation, which however is mainly due to the compression of the high aspect ratio for visual clarity. While such variation influence the local contact angle of the working fluid, the effect is minimal. For the water-copper heat pipe used, the minimum contact angle is $\theta_{min} = 33^\circ$, and even in the worst-case scenario, width variation alters the contact angle by less than 0.05° . This corresponds to a change of approximately 1 percent and therefore considered negligible in the model.

This improvement highlights the importance of groove geometry in enhancing thermal performance. To better understand the mechanisms behind this behavior, it is useful to examine the internal flow characteristics of the optimized wick structure. The vapor and liquid velocities, meniscus curvature, and solid temperature distributions provide insight

Table 4

Maximum heat input and the optimized wick structures improvement wrt. reference FMHP.

	Q_{in} [W]	Improvement [%]
Straight Reference	89.43	–
Converging	109.88	22.87
Optimized, $W_{min} = 160\mu\text{m}$	111.00	24.12
Optimized, $W_{min} = 60\mu\text{m}$	191.32	113.93

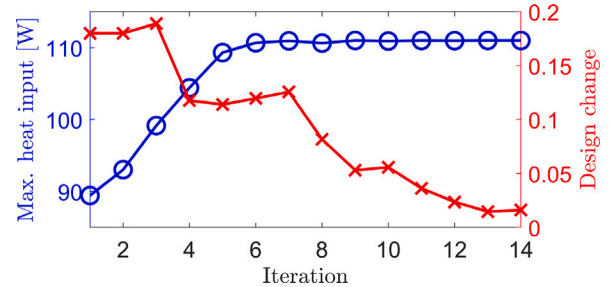


Fig. 12. Objective evolution with maximum per iteration change of the design variables.

into how the groove shape influences fluid transport and heat transfer, which is discussed in the following

The axial mass flux, ρAu , for both liquid and vapor are shown in the top of Fig. 13, along with the net axial mass flux, which remains zero throughout the heat pipe.

During evaporation, the vapor axial mass flux increases monotonically. In the adiabatic section, it remains constant, while in the condensation region, it decreases monotonically. This behavior is characteristic of conventional heat pipes and is also observed for the optimized wick structure in the middle of Fig. 13.

Since the vapor cross sectional area is constant, the mean vapor velocity exhibits the same spatial variation as the vapor axial mass flux, differing only by the constant scaling factor of the cross-sectional area. In contrast, the groove width and therefore the liquid cross sectional area vary along the heat pipe. For the approximately constant liquid axial mass flux between $x/L_t = 0.25$ and $x/L_t = 0.6$, a significant reduction in u_l is seen, which occurs due to the expansion of the groove width. The expansion increases the liquid cross sectional area, thereby reducing the liquid pressure drop, but at the cost of higher shear stress along the liquid vapor meniscus.

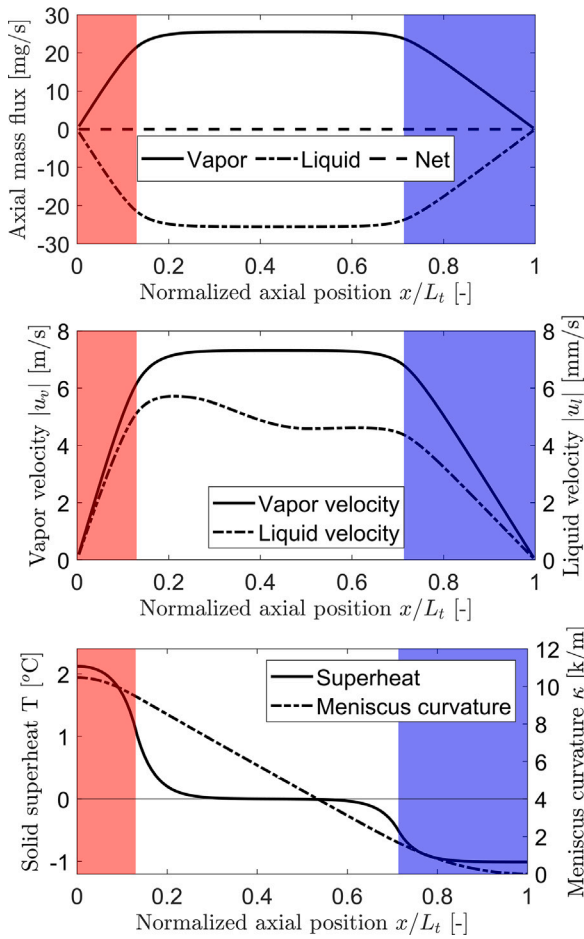


Fig. 13. Axial mass fluxes, velocities, superheat of solid and curvature of meniscus for the optimized grooved wick structure.

Due to the boundary conditions on the curvature of meniscus the heat pipe is essentially limited to a fixed capillary pressure, which in turn drives the optimization to minimize internal pressure drop in both vapor and liquid. The simplest way of achieving a lower pressure drop is to reduce the mean fluid velocity, which leads to the wide groove in the condenser half. However, due to the presence of the vapor induced shear stress acting on the meniscus and limitation of a minimum contact angle for fluid–solid combination it is not ideal to maximize groove width throughout the wick structure.

To maximize the available capillary pressure the difference between maximum and minimum curvature must be maximized. This leads to the groove width at the evaporator end being minimized, which maximizes the curvature for a fixed contact angle as shown in (18). Due to the prescribed curvature in the condenser end, the optimizer can prioritize the pressure drop over the curvature effect near the condenser end, which leads to a wide groove.

Due to the constraint of a minimum contact angle throughout the heat pipe, the groove width expansion from the evaporator end is limited to ensure $W_f/(2\kappa)$ does not exceed $\cos \gamma_{min}$ anywhere. Therefore, a non-linear expansion appears instead of a constant expansion rate.

3.2.2. Influence of working temperature

This section covers the effect of working temperature on the optimized grooved wick structure and maximum heat input. The working temperature affects the material properties of the working fluid.

For comparison both the maximum heat input of the optimized wick structure and the uniform wick structure are shown in Fig. 14. As the

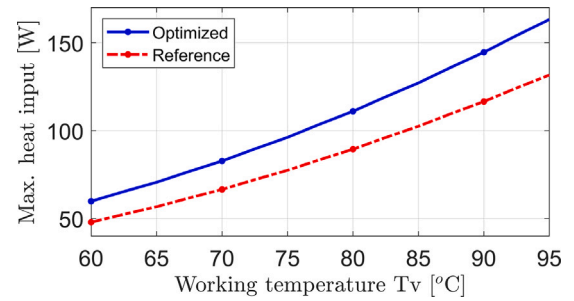


Fig. 14. Effect of working temperature on optimized and reference heat pipe performance.

working temperature increases the maximum heat input increases for both the reference and optimized wick structures.

Fig. 15 shows that higher T_v leads to a generally wider groove in the optimized distribution, but the non-linear expansion at the evaporator end is maintained.

The most notable effect of changing T_v is the vapor density, which leads to a lower density ratio for increasing T_v as shown in Fig. 16.

As vapor density increases, the vapor velocity u_v decreases for a given mass flux. This in turn reduces the vapor wall shear stress τ_{vw} , which leads to a reduction in fRe .

Owing to the reduced meniscus shear stress at elevated vapor temperatures, a wider groove becomes favorable. The increased groove width decreases the liquid velocity u_l , thereby reducing the liquid pressure drop. This enables a greater portion of the total pressure drop to be utilized for increasing heat transfer, resulting in a higher heat input. Consequently, the optimal groove width increases with rising vapor temperature T_v .

3.2.3. Influence of number of design variables

This section covers the effect of changing the number of design variables, n_ψ , in the optimization problem. The effect on the optimized wick structure and maximum heat input is examined. The reference heat pipe is used as the initial wick structure with groove width upper and lower limits from Table 3. The number of design variables, n_ψ , is swept from one to twelve. The lower limit is a uniform groove. The upper limit was set to twelve to balance computational efficiency with design resolution and large n_ψ increases computational effort and exploit modeling simplifications.

The improvement in the objective function i.e. maximum heat input, wrt. the maximum heat input for the reference heat pipe, indicates a small increase in the maximum heat input for increasing n_ψ , as seen in Fig. 17.

Despite the small improvement in maximum heat input, a significant change in groove width distribution for sweeping n_ψ is observed in Fig. 18. For $n_\psi > 1$ the evaporator end is narrow while the condenser end is wide. As n_ψ increases, the wide region of groove grows in length. This indicates that a higher resolution allows for quicker change in groove width without violating the contact angle boundary condition.

A combination of the decreasing improvement in maximum heat input and the significant changes in optimized groove width distribution for increasing n_ψ indicates that it is not important to use large numbers of design variables. Furthermore, it indicates that the most important feature in the optimized wick structure is the narrow evaporator end and wide groove away from the region of evaporation. Which is similar to the observation for variations in T_v .

While increasing the number of design variables refines the groove profile, the improvement in thermal performance plateaus beyond moderate resolutions. This suggests that the dominant design features are captured with relatively few parameters, enabling a favorable trade-off between computational cost and design fidelity.

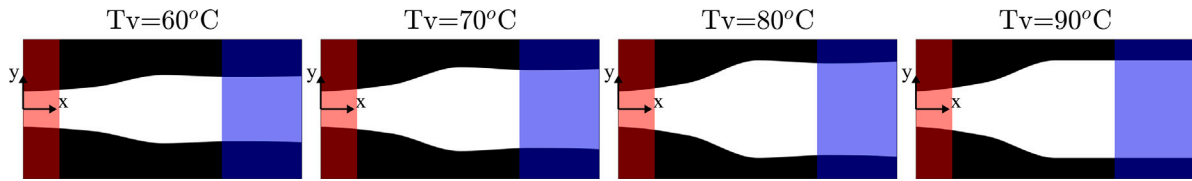


Fig. 15. Effect of working temperature on optimized wick structure.

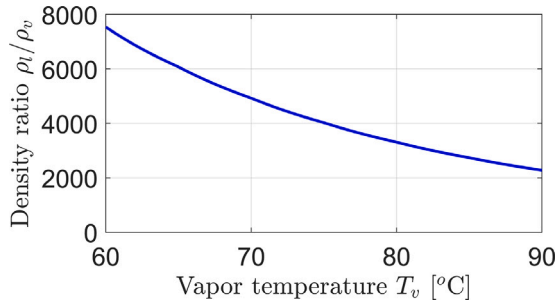


Fig. 16. Effect of T_v on density ratio.

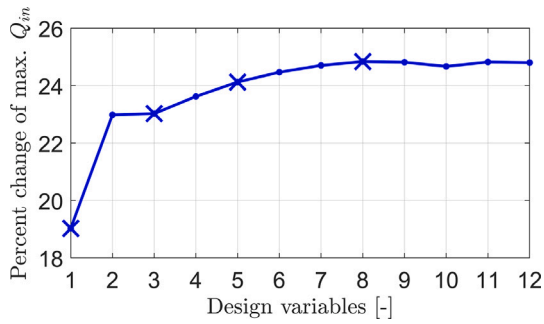


Fig. 17. Effect of n_ψ on percent improvement of maximum heat input wrt. optimized maximum heat input for $n_\psi = 3$. Crosses refer to designs shown in Fig. 18.

3.2.4. Influence of evaporator to length ratio

This section examines the effect of changing the evaporator length L_e for the reference heat pipe and its effects on maximum heat input and optimized wick structure.

The maximum heat input increases for increasing L_e , as shown in Fig. 19. For a fixed wick structure and heat input the effect of increasing the length of the evaporator is a larger region of evaporation, which in turn leads to lower velocity gradients for both vapor and liquid in the region of evaporation. These reduced slopes of velocities lead to a lower average value of vapor and liquid velocities, which is reflected in lower pressure gradients and reduced meniscus shear stress. These reductions allow for a higher maximum heat input as the evaporation region increases in length.

The increase in maximum heat input in Fig. 19 can partially be explained by the shorter effective length, $L_{eff} = L_e/2 + L_a + L_c/2$, since the capillary limit for a fixed geometry is inversely proportional to L_{eff} .

For the L_e sweep significant change to the optimized groove wick structure is seen in Fig. 21, which indicates that the groove width distribution within the evaporation region is important for maximum heat input.

For L_c sweep no difference was found in the optimized groove wick structure, but the maximum heat input showed inverse proportional scaling with L_{eff} .

As the evaporator length L_e increases, the region along the groove with near minimum width becomes longer. This is because the optimization seeks to maximize capillary pressure while adhering to the constraint imposed by the minimum allowable contact angle.

To achieve maximum capillary pressure at the evaporator, the groove width is constrained to its minimum value W_{min} . The minimum contact angle condition is expressed as:

$$\cos \gamma_{min} = \frac{1}{2} W_f \kappa \quad (23)$$

where γ_{min} is determined by the fluid–solid material combination. Eq. (23) implies that this constraint is only satisfied if the increase in groove width is sufficiently gradual compared to the decrease in curvature along the groove axis.

Since smaller groove widths increase the liquid pressure drop, the optimizer must balance the effects of capillary performance and hydraulic losses. This is accomplished by controlling the axial gradient of the groove width $\frac{\partial W_f}{\partial x}$, ensuring that the groove widens gradually so that the contact angle condition remains satisfied. This behavior is shown in Fig. 20.

For short evaporator lengths, the term $\frac{1}{2} W_f \kappa$ remains below $\cos \gamma_{min}$, indicating that the contact angle constraint is inactive. For longer evaporator lengths, $\frac{1}{2} W_f \kappa$ approaches $\cos \gamma_{min}$, activating the constraint. As a result, the optimizer reduces the rate of groove widening to avoid violating the contact angle limit.

The evaporator end geometry plays a critical role in determining the thermal performance of FMHPs due to the intrinsic coupling between groove width and meniscus curvature. Capillary pressure is increased by a narrow groove at the evaporator end. However, the ability to widen the groove upstream to lower hydraulic resistance is constrained by the minimum contact angle. Since the contact angle is a function of groove width and meniscus curvature, the optimizer must ensure that the axial gradient of the groove width is matched by a corresponding gradient in curvature to maintain physical feasibility. This coupling imposes a geometric constraint on the rate of groove expansion, effectively linking the shape of the groove to the development of the meniscus. As a result, the optimized designs exhibit nonlinear groove profiles that balance capillary performance with hydraulic resistance, particularly in the evaporator region where thermal demands are highest.

4. Conclusion

This study presents a numerical model for fast and sufficiently accurate prediction of the thermal performance of flat miniature heat pipes with a non-uniform rectangular grooved wick structure.

Simplifying the physics by decoupling meniscus curvature from the mass and momentum equations and by linearizing the nonlinear phase-change mass flux significantly reduced the evaluation time while maintaining a high level of accuracy. The proposed numerical model shows decent agreement with both experimental and numerical studies, [7,9].

The model was successfully applied to optimize groove width distributions for maximum heat input. The results demonstrate that significant performance gains can be achieved through shape optimization,

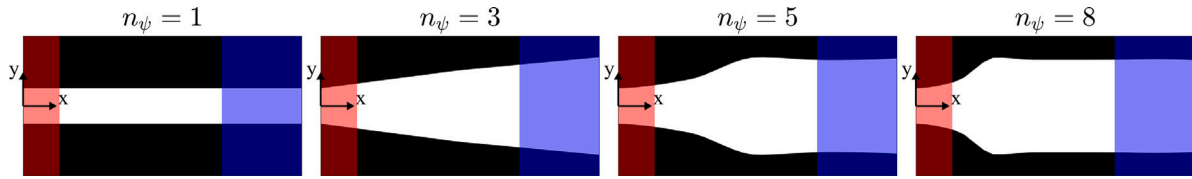


Fig. 18. Effect of n_ψ on optimized wick structure.

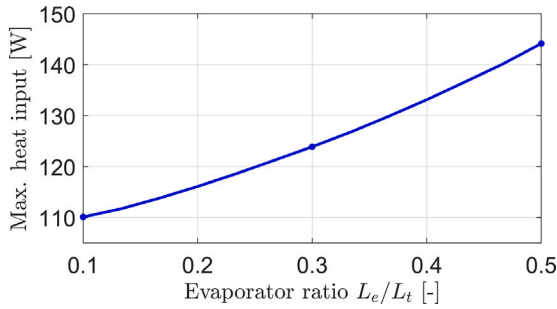


Fig. 19. Effect of L_e/L_t on the maximum heat input of the optimized heat pipe.

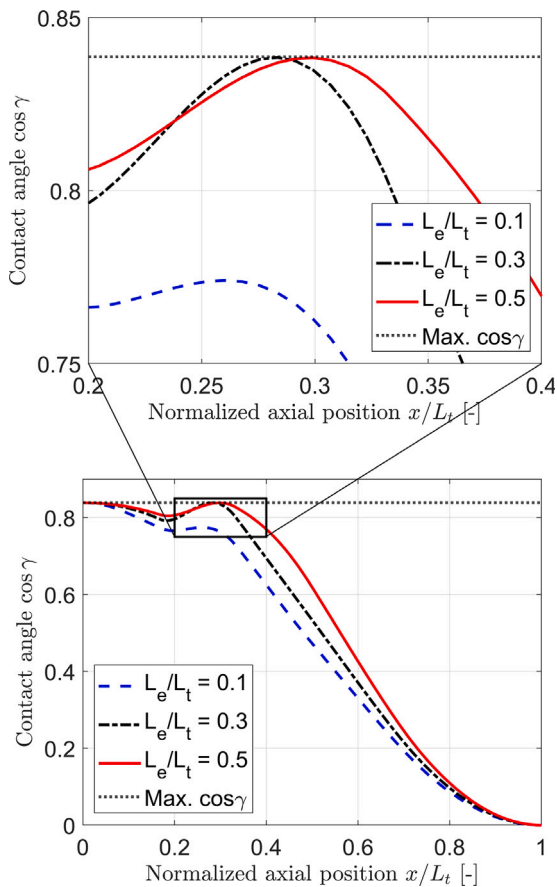


Fig. 20. Axial variation of contact angle for various L_e/L_t .

with improvements of up to 24% over conventional uniform designs and modest gains over previously proposed converging geometries.

The thermal performance of optimized FMHPs is strongly influenced by the working temperature. Higher operating temperatures increase vapor density, which reduces shear stress and allows for wider grooves

without compromising capillary performance. This temperature-dependent behavior suggests that further gains can be achieved by adapting groove geometries to specific thermal conditions, particularly in the condenser region where geometric freedom is underutilized.

The optimized wick structure shows a strong dependency on evaporator length, reinforcing the importance of geometric constraints in high-performance FMHP design. Longer evaporators result in an extended region of near-minimum groove width near the evaporator due to the constraint imposed by the minimum contact angle.

4.1. Future work

As the proposed model is greatly simplified and developed from models for uniform wick structures, it is planned to perform experimental verification of the optimized wick structure against the uniform reference and converging wick structures.

CRediT authorship contribution statement

Asger Bjerregaard Petersen: Writing – original draft, Visualization, Software, Methodology, Formal analysis. **Ole Sigmund:** Writing – review & editing, Visualization, Supervision, Conceptualization. **Casper Schousboe Andreassen:** Writing – review & editing, Visualization, Validation, Supervision, Software, Conceptualization.

Declaration of competing interest

The authors declare that they have no known competing financial interests or personal relationships that could have appeared to influence the work reported in this paper.

Acknowledgments

We would like to thank Ali Mostafazade Abolmaali, Mohamad Bayat and Jesper Hattel for useful discussions and support. We gratefully acknowledge financial support from the Independent Research Fund Denmark through the DFF-FTP2 Extreme Heat project (Contract No. 2035-00193B).

Appendix. Material properties

In this appendix the full table of material properties are given. The properties are limited to only depend on the working temperature of the vapor T_v . For values of T_v in between the given data points a cubic interpolation scheme is used to generate material properties. In no parts of the paper is the working temperature set outside the data in Table A.5.

Data availability

Data will be made available on request.

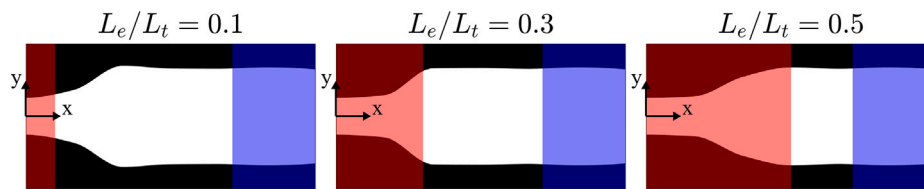


Fig. 21. Effect of L_e/L_t on the optimized wick structure.

Table A.5

Complete data for material properties.

T_v °C	ρ_l kg m ⁻³	ρ_v kg m ⁻³	μ_l μPa s	μ_v μPa s	σ mN m ⁻¹	h_{fg} MJ kg ⁻¹
60	983.16	0.13043	466	10.9	66.238	2.3576
65	980.52	0.16146	433	11.0	65.366	2.3454
70	977.73	0.19843	404	11.2	64.481	2.3330
75	974.81	0.24219	377	11.4	63.583	2.3206
80	971.77	0.29367	354	11.5	62.673	2.3080
85	968.59	0.35388	333	11.7	61.750	2.2953
90	965.3	0.42390	314	11.9	60.816	2.2825
95	961.88	0.50491	297	12.1	59.870	2.2695

References

- [1] iNEMI, Electronics manufacturing initiative technology roadmap, 2004.
- [2] A. Faghri, Heat Pipe Science and Technology, second ed., Global Digital Press, 2016.
- [3] T.P. Cotter, Principles and prospects for micro heat pipes, in: Proc. 5th Int. Heat Pipe Conf., 1984, pp. 328–335.
- [4] B.R. Babin, G.P. Peterson, D. Wu, Steady-state modeling and testing of a micro heat pipe, J. Heat Transf. (1990).
- [5] D. Khristalev, A. Faghri, Thermal analysis of a micro heat pipe, J. Heat Transfer-Trans. the ASME 116 (1) (1994) 189–198.
- [6] D. Khristalev, A. Faghri, Thermal characteristics of conventional and flat miniature axially grooved heat pipes 1, J. Heat Transf. 117 (1995) 1048–1054.
- [7] R. Hopkins, A. Faghri, D. Khristalev, Flat miniature heat pipes with micro capillary grooves, J. Heat Transf. 121 (1999) 102–109.
- [8] K.H. Do, S.J. Kim, S.V. Garimella, A mathematical model for analyzing the thermal characteristics of a flat micro heat pipe with a grooved wick, Int. J. Heat Mass Transfer 51 (19–20) (2008) 4637–4650, <http://dx.doi.org/10.1016/j.ijheatmasstransfer.2008.02.039>.
- [9] A. Mostafazade Abolmaali, M. Bayat, J. Hattel, Advancing thermohydraulic performance of micro-grooved flat heat pipes through a combined numerical-experimental approach, Appl. Therm. Eng. 258 (2025) 124606, <http://dx.doi.org/10.1016/j.applthermaleng.2024.124606>.
- [10] A. Mostafazade Abolmaali, M. Bayat, J. Hattel, A multiscale analytical-numerical method for the coupled heat and mass transfer in the extended meniscus region considering thin-film evaporation in microchannels, Int. J. Heat Mass Transfer 222 (2024) <http://dx.doi.org/10.1016/j.ijheatmasstransfer.2023.125145>.
- [11] A. Mostafazade Abolmaali, M. Bayat, J. Hattel, Thin-film evaporation in microchannels: A combined analytical and computational fluid dynamics approach to assessing meniscus curvature impact, Int. J. Therm. Sci. 208 (2025) 109455, <http://dx.doi.org/10.1016/j.ijthermalsci.2024.109455>.
- [12] G. Gökçe, C. Kurt, G. Odabaşı, Z. Dursunkaya, B. Çetin, Comprehensive three-dimensional hydrodynamic and thermal modeling of steady-state operation of a flat grooved heat pipe, Int. J. Multiph. Flow 160 (2023) <http://dx.doi.org/10.1016/j.ijmultiphaseflow.2022.104370>.
- [13] G. Gökçe, B. Çetin, Z. Dursunkaya, Accelerated 3D CFD modeling of multichannel flat grooved heat pipes, Energy 305 (2024) <http://dx.doi.org/10.1016/j.energy.2024.132289>.
- [14] W.Z. Fang, Y.Q. Tang, C. Yang, W.Q. Tao, Numerical simulations of the liquid-vapor phase change dynamic processes in a flat micro heat pipe, Int. J. Heat Mass Transfer 147 (2020) <http://dx.doi.org/10.1016/j.ijheatmasstransfer.2019.119022>.
- [15] T. Alam, U. Upadhyay, S. Azam, R. Kumar, Heat pipe mass optimization for space applications, in: 3rd Int'L Conf. Recent Advances in Information Technology RAIT-2016, IEEE, 2016.
- [16] T. Dbouk, A review about the engineering design of optimal heat transfer systems using topology optimization, Appl. Therm. Eng. 112 (2017) 841–854, <http://dx.doi.org/10.1016/j.applthermaleng.2016.10.134>.
- [17] Z.J. Xu, M.S. Luo, Q.H. Wang, H. Zhao, Y.J. Wang, D.X. Deng, Shape optimization of composite porous vapor chamber with radial grooves: A study on the minimization of maximum pressure drop, Appl. Therm. Eng. 201 (2022) <http://dx.doi.org/10.1016/j.applthermaleng.2021.117735>.
- [18] D.J. Lohan, S.N. Joshi, E.M. Dede, Evaluation of vapor chambers incorporating square-shaped and topology optimized pedestals, in: InterSociety Conference on Thermal and Thermo-mechanical Phenomena in Electronic Systems, IThERM, IEEE Computer Society, 2024, <http://dx.doi.org/10.1109/IThERM55375.2024.10709613>.
- [19] S.A. Lurie, L.N. Rabinskiy, Y.O. Solyaev, Topology optimization of the wick geometry in a flat plate heat pipe, Int. J. Heat Mass Transfer 128 (2019) 239–247, <http://dx.doi.org/10.1016/j.ijheatmasstransfer.2018.08.125>.
- [20] P.C. Stephan, C.A. Busse, Analysis of the heat transfer coefficient of grooved heat pipe evaporator walls, Int. J. Heat Mass Transfer 35 (2) (1992) 383–391.
- [21] F. Lefèvre, R. Rullière, G. Pandraud, M. Lallemand, Prediction of the temperature field in flat plate heat pipes with micro-grooves - experimental validation, Int. J. Heat Mass Transfer 51 (15–16) (2008) 4083–4094, <http://dx.doi.org/10.1016/j.ijheatmasstransfer.2007.12.007>.
- [22] J.P. Longtin, B. Badran, A one-dimensional model of a micro heat pipe during steady-state operation, J. Heat Transf. (1994) 709–715.
- [23] F. White, J. Majdalani, Viscous Fluid Flow, McGraw-Hill New York, 2006.
- [24] G.E. Schneider, R. DeVos, Nondimensional analysis for the heat transfer capability of axially-grooved heat pipes including liquid/vapor interaction, 1980, AIAA Paper 80-0214.
- [25] R.K. Shah, A.L. London, Laminar Flow Forced Convection in Ducts, Academic Press, 1978.
- [26] R. Rullière, F. Lefèvre, M. Lallemand, Prediction of the maximum heat transfer capability of two-phase heat spreaders - experimental validation, Int. J. Heat Mass Transfer 50 (7–8) (2007) 1255–1262, <http://dx.doi.org/10.1016/j.ijheatmasstransfer.2006.09.015>.
- [27] C. Le, T. Bruns, D. Tortorelli, A gradient-based, parameter-free approach to shape optimization, Comput. Methods Appl. Mech. Engrg. 200 (9–12) (2011) 985–996, <http://dx.doi.org/10.1016/j.cma.2010.10.004>.
- [28] F.N. Fritsch, R.E. Carlson, Monotone piecewise cubic interpolation, SIAM J. Numer. Anal. 17 (2) (1980) 238–246.
- [29] K. Svanberg, The method of moving asymptotes - a new method for structural optimization, Internat. J. Numer. Methods Engrg. 24 (1987) 359–373.
- [30] W. Squire, G. Trapp, Using complex variables to estimate derivatives of real functions digital commons citation, SIAM Rev. 40 (1998) 110–112.